Nano Research
2023, 16(3): 3879–3887

ISSN 1998-0124 CN 11-5974/O4
https://doi.org/10.1007/s12274-023-5540-2

Research Article

Controllable assembly of nitrogen-doped mesoporous carbon with different pore structures onto CNTs for excellent lithium storage

Haitao Li[1], Xiao Fang[2], Fengting Lv[1], Wei Yu[2], Hui Cheng[1], and Haijiao Zhang[1,3] (✉)

[1] *Institute of Nanochemistry and Nanobiology, School of Environmental and Chemical Engineering, Shanghai University, Shanghai 200444, China*
[2] *School of Environmental and Materials Engineering, College of Engineering, Shanghai Polytechnic University, Shanghai 201209, China*
[3] *Key Laboratory of Advanced Energy Materials Chemistry (Ministry of Education), Nankai University, Tianjin 300071, China*

Received: 16 January 2023 / **Revised:** 30 January 2023 / **Accepted:** 31 January 2023

ABSTRACT

Mesoporous carbon nanomaterials have shown a great application potential in energy storage and conversion fields due to their outstanding conductivity, tunable pore structure, and good chemical stability. Nevertheless, how to accurately control the pore structure, especially directly assembling the mesoporous carbon onto different substrates remains a big challenge. Herein, we have successfully assembled two kinds of highly nitrogen-doped mesoporous carbon onto carbon nanotubes (NMC/CNTs) based on a facile cooperative assembly process assisted by triblock $PEO_{20}PPO_{70}PEO_{20}$ (P123) and $PEO_{106}PPO_{70}PEO_{106}$ (F127) copolymers. The experimental results indicate that the P123/F127 mass ratio has a profound effect on the pore structure, leading to the formation of NMC/CNTs composites with spherical pore structure (S-NMC/CNTs) and cylindrical pore structure (C-NMC/CNTs). In virtue of fast electron/ion transfer kinetics, the as-prepared S-NMC/CNTs anode demonstrates an excellent electrochemical performance for lithium-ion batteries, and it delivers a high reversible capacity of 588.1 mAh·g^{-1} at the current of 0.1 A·g^{-1} after 100 cycles, along with a superior cycling stability. Specifically noted, the controlled assembly route developed in our work can also be applied to other support materials with different structures and compositions.

KEYWORDS

mesoporous carbon, carbon nanotubes, controllable assembly, formation mechanism, lithium-ion batteries

1 Introduction

In recent years, the wide applications of electric vehicles, portable electronic products, and wearable electronic devices in the consumer market have greatly promoted the development of lithium-ion batteries (LIBs) [1–3]. In turn, that also puts forward higher requirement for high-energy LIBs. The commercial graphite anode material most commonly used in LIBs cannot meet the market demand due to its low theoretical capacity of 372 mAh·g^{-1} [4]. Therefore, it is urgent to develop suitable anode materials with higher capacities to meet the increasing energy demand [5–7].

In these available anodes, mesoporous carbon materials have shown a wide application prospect in energy storage fields, such as rechargeable secondary batteries and supercapacitor, due to their large specific surface area, adjustable pore size/structure, high electrical conductivity, and superior chemical stability [8–12]. For example, Guo's group prepared ordered mesoporous carbon, which was used as the anode material for LIBs [13]. Thanks to the unique ordered mesoporous structure, the obtained electrode showed excellent electrochemical performance for LIBs. Besides, mesoporous carbon can be directly assembled onto other substrates to further improve the energy storage performance. Yamauchi et al. prepared mesoporous carbon@MXene composite via a composite–micelle-directed interfacial assembly method [14]. The existence of mesoporous structure in the composite can not only effectively increase sulfur loading, but also well alleviate the volume expansion during the charging/discharging process. Therefore, when employed as the cathode for Li-S batteries, it delivered a high reversible capacity of 914 mAh·g^{-1} after 500 cycles at the current density of 0.5 C, which was superior to those of non-porous composites. Although important progress has been made in the assembly of mesoporous carbon onto different substrates, recent researches mainly focus on the assembly of two-dimensional (2D) mesoporous structure [15–18]. In contrast, one-dimensional (1D) structure has shown its unique structural advantage in energy storage applications owing to larger aspect ratio and faster electron/ion transfer rate [19–23]. However, there are few studies on the assembly of mesoporous carbon onto carbon nanotubes (CNTs). Besides, the pore structure is directly related to the electrochemical performance of electrode materials [24, 25]. Therefore, it remains a major challenge to prepare the mesoporous carbon with controllable pore structure onto CNTs. On the other hand, the introduction of nitrogen atoms into carbon material can not only provide more defects, but also effectively increase the conductivity of the electrode, thus boosting the electrochemical storage performance [26, 27].

Herein, we present a facile cooperative co-assembly strategy for preparation of two kinds of N-doped mesoporous carbon (NMC) with different pore structures, which are *in-situ* assembled onto the surface of CNTs by using $PEO_{20}PPO_{70}PEO_{20}$ (P123) and $PEO_{106}PPO_{70}PEO_{106}$ (F127) as soft templates and melamine-formaldehyde (MF) resins as the precursor. Importantly, the pore

Address correspondence to hjzhang128@shu.edu.cn

structure of NMC can be easily turned from spherical to cylindrical only by adjusting the mass ratio of P123 and F127. Finally, the obtained two NMC/CNTs composites are used as the anode materials in LIBs to study the effect of pore structure on their energy storage performances. The electrochemical tests indicate that the NMC/CNTs anode with spherical pore structure (S-NMC/CNTs) exhibits a better lithium storage performance due to faster electron and ion transfer kinetics compared with NMC/CNTs with cylindrical pore structure (C-NMC/CNTs).

2 Experimental

2.1 Materials

Triblock copolymers Pluronic F127 (M_W = 12,600), $PEO_{133}PPO_{50}PEO_{133}$ (F108, M_W = 14,600), and P123 (M_W = 5800) were purchased from Sigma-Aldrich. HCl, NaOH, melamine, and formaldehyde solution (37 wt.% in water) were provided by Chinese Sinopharm Chemical Reagent Co. Deionized water was applied in all the experiments.

2.2 Acid treatment of CNTs

250 mg of CNTs were ultrasonically dispersed in 30 mL of concentrated H_2SO_4 and 10 mL of HNO_3, stirred in an oil bath at 60 °C for 3 h, then washed to neutral with deionized water and filtered to collect the products. Finally, the acid-treated CNTs were obtained after vacuum freeze-dried.

2.3 Preparation of MF resin oligomers

The MF resin solutions were prepared according to previous work [9, 28]. Typically, 252 mg of melamine and 640 μL of formaldehyde were mixed in 40 mL of deionized water. Then, 0.05 mL of NaOH solution (0.1 M) was added and stirred for 30 min at 70 °C and then cooled down to obtain the MF resin oligomer solution.

2.4 Synthesis of NMC/CNTs composites

Two kinds of NMC/CNTs products with different pore structures were prepared based on a facile cooperative assembly process. The NMC/CNTs product with spherical pore structure was prepared as follows: Typically, 0.15 g of P123 and 0.15 g of F127 were added to 10 mL of deionized water and stirred for 30 min at 40 °C. Then, 12 mg of acid-treated CNTs were added into the above solution under stirring for another 30 min. After increased the reaction temperature to 55 °C, the above MF resin oligomer solution and 0.6 mL of HCl (0.1 M) were further added and kept stirring for 12 h. Subsequently, the gray precipitate was harvested by centrifugation and washing with ethanol and deionized water several times and drying for 12 h at 60 °C. Finally, the as-prepared product was further heated at 500 °C with a temperature increasing rate of 2 °C·min^{-1} for 1 h under N_2 atmosphere. And another C-NMC/CNTs product with cylindrical pore structure was also synthesized following the similar procedure except for the addition of F127. Besides, the control sample of N-doped carbon (NC)/CNTs was also prepared similar to the above procedure with the absence of F127 and P123.

2.5 Structural characterizations

The crystal structure, chemical state, and elemental composition of the samples were systematically investigated by powder X-ray diffraction (XRD, RigaKu D/max-2550), Raman spectra (InVia 25LM06), and Fourier transform infrared (FT-IR) spectrometer (EDK 9500). Scanning electron microscopy (SEM, Zeiss SUPRA 55) and transmission electron microscopy (TEM, Hitachi HT7700) were conducted to observe the delicate microstructure of the samples. The energy-dispersive X-ray (EDX) analysis was conducted on Zeiss SUPRA 55. N_2 adsorption/desorption isotherms were collected on a QUADRASORB SI surface area and pore size analyzer at 77 K. Before analysis, the samples were degassed under vacuum at 100 °C for 12 h. The thermal stability was analyzed using thermogravimetric analysis (TGA) apparatus (NETZSCH STA 449F5), and the samples were heated to 800 °C in N_2 with a heating rate of 10 °C·min^{-1}. The surface electrical properties of samples were also tested on Malvern Zetasizer Nano S.

2.6 Electrochemical measurements

The working electrode was fabricated by blending the active material with acetylene black (super-p) and polyvinylidene fluoride (PVDF) at a weight ratio of 8:1:1 in N-methyl-2-pyrrolidinone to obtain the homogeneous slurry. Then, the slurry was painted onto the copper foil, which was dried at 70 °C for 12 h in a vacuum oven. The electrochemical performances were evaluated by using CR2032 coin-type half-cells, and Li foil was acted as both counter and reference electrodes. The electrolyte was composed of 1 M $LiPF_6$ in ethylene carbonate/dimethyl carbonate (EC/DEC, v/v = 1/1). The mass loading of the active material was 0.8–1.2 mg·cm^{-2}. The cells were assembled in an Ar-filled glovebox with high purity at room temperature. The galvanostatic charge/discharge cycles were collected with a LAND CT2001A Battery Tester between 0.01 and 3.00 V at a constant current density. The cyclic voltammetry (CV) curves and electrochemical impedance spectroscopy (EIS) results were obtained in a CHI 660E potentiostat/galvanostatic electrochemical workstation.

3 Results and discussion

The synthetic procedures of NMC/CNTs composites with different pore structures are illustrated in Fig. 1. The acid-treated CNTs were first dispersed in the micelle solution of triblock copolymers, and the micelles were then deposited onto the CNT surface. Afterwards, MF resin oligomers were further added and the co-assembly behavior began to occur among CNTs, micelles, and oligomers due to the hydrogen bonding and electrostatic interactions [29]. Finally, the NMC/CNTs composites with different pore structures were obtained after carbonization under nitrogen atmosphere.

The structures of as-synthesized mesoporous MF/CNTs composites with different pore structures were first characterized by SEM and TEM techniques. Figure 2(a) displays the SEM image of mesoporous MF/CNTs composite with spherical pore (S-MF/CNTs), it can be clearly seen that the resulting composite exhibits a uniform 1D structure similar to that of CNTs (Fig. S1 in the the Electronic Supplementary Material (ESM)). The diameter is significantly increased to about 82 nm, compared with 15 nm of individual CNTs. Additionally, the uniform spherical pores are arranged onto the surface of CNTs. The TEM image of S-MF/CNTs further demonstrates the 1D mesoporous structure (Fig. 2(e)). These phenomena indicate that the effective co-assembly has perfectly performed among CNTs, micelles, and MF resin. After carbonization at 500 °C, the diameter of S-NMC/CNTs is reduced to 42 nm (Figs. 2(b) and 2(f)). These results indicate that there are some obvious structural contractions during the carbonization process, corresponding to a shrinkage rate of 49%. Figure 2(c) shows the SEM image of mesoporous MF/CNTs composite with cylindrical pore (C-MF/CNTs), and it shows a similar 1D structure to S-MF/CNTs, with an average diameter of 54 nm. Differently, cylindrical pores are closely arranged onto the CNT surface, as can be observed from the TEM image in Fig. 2(g). Similarly, the diameter of C-NMC/CNTs is

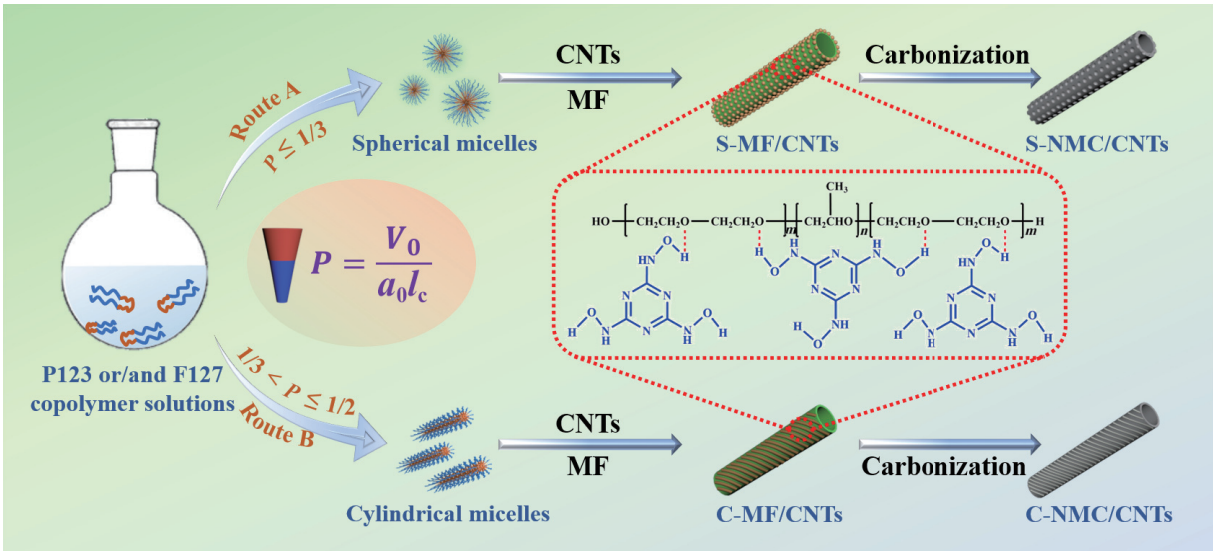

Figure 1 Schematic illustration of synthetic processes of S-NMC/CNTs and C-NMC/CNTs composites.

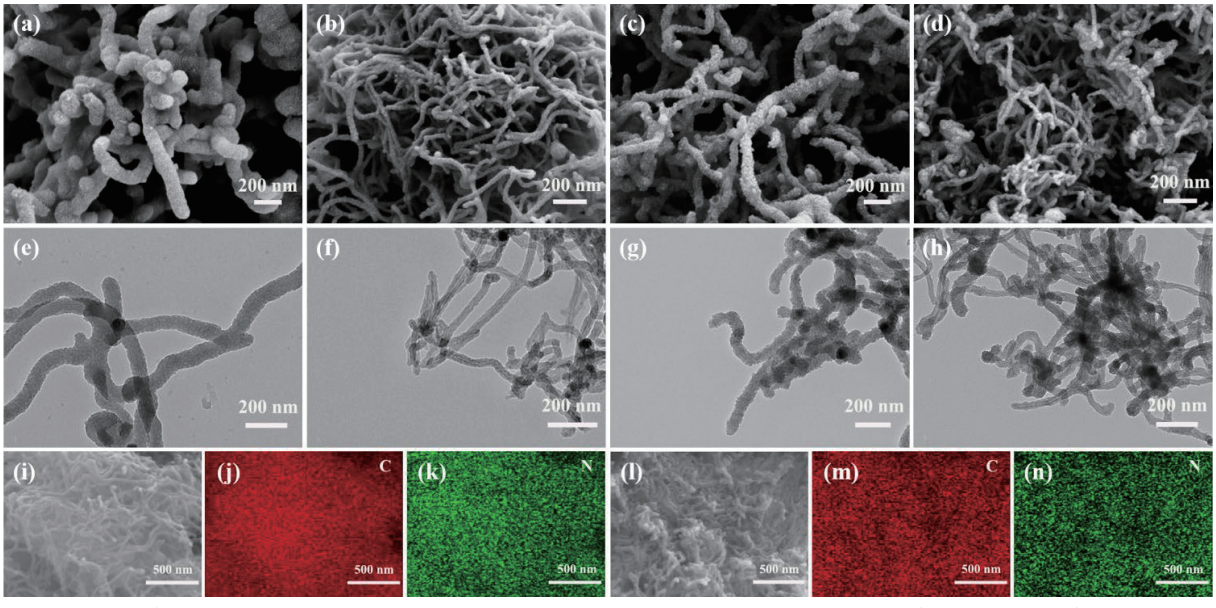

Figure 2 SEM images of (a) S-MF/CNTs, (b) S-NMC/CNTs, (c) C-MF/CNTs, and (d) C-NMC/CNTs. TEM images of (e) S-MF/CNTs, (f) S-NMC/CNTs, (g) C-MF/CNTs, and (h) C-NMC/CNTs. (i)–(k) STEM image and elemental mappings of S-NMC/CNTs. (l)–(n) STEM image and elemental mappings of C-NMC/CNTs.

decreased to about 28 nm, possessing a shrinkage rate of 48% after carbonization (Figs. 2(d) and 2(h)). The scanning TEM (STEM) images and elemental mappings of S-NMC/CNTs (Figs. 2(i)–2(k)) and C-NMC/CNTs (Figs. 2(l)–2(n)) display that the C and N elements are homogeneously distributed on the whole CNTs. Meanwhile, the EDX analysis shows that the nitrogen contents of S-NMC/CNTs and C-NMC/CNTs are 47.6% and 42.3%, respectively (Figs. S2(a) and S2(b) in the ESM). Such a high nitrogen doping is beneficial to the improvement of conductivity and electrochemical performances of the electrode materials.

Figure 3(a) shows the XRD patterns of two products. As can be seen, both S-NMC/CNTs and C-NMC/CNTs exhibit two broad diffraction peaks at 23.5° and 43.7°, which can be assigned to the (002) and (100) crystal planes of carbon materials, indicating an amorphous carbon structure [30, 31]. Raman technique was further used to analyze the structures of two composites. As shown in Fig. 3(b), there are two strong characteristic peaks at 1302 and 1579 cm^{-1}, corresponding to the disordered carbon (D band) and graphitization carbon (G band), respectively [32]. The I_D/I_G values of S-NMC/CNTs and C-NMC/CNTs were calculated to be 1.42 and 1.43, suggesting that the obtained NMC/CNTs composites possess the large number of defects.

N_2 adsorption/desorption isotherms were measured to analysis the textural properties of the samples. As displayed in Figs. 3(c) and 3(d), both S-NMC/CNTs and C-NMC/CNTs composites demonstrate the type IV hysteresis loop at the relative pressure of $0.45 < P/P_0 < 0.85$, indicating the presence of mesoporous structures [33, 34]. The Barrett–Emmett–Teller (BET) surface area and pore volume of S-NMC/CNTs are 187.9 $m^2 \cdot g^{-1}$ and 0.31 $cm^3 \cdot g^{-1}$, respectively. For C-NMC/CNTs, the specific surface area and pore volume increase to 249.6 $m^2 \cdot g^{-1}$ and 0.41 $cm^3 \cdot g^{-1}$. The larger surface area of C-NMC/CNTs can be attributed to the more open structure caused by the cylindrical pore. Meanwhile, the average pore sizes of S-NMC/CNTs and C-NMC/CNTs composites are 3.9 and 4.0 nm, respectively (insets of Figs. 3(c) and 3(d)). The narrow pore size and high surface area are conducive to the transport of electrons and ions, as well as the full infiltration of electrodes and electrolytes, so as to improve the performance of lithium storage.

The thermal stability of the as-prepared MF/CNTs composites was explored via TGA technique under nitrogen atmosphere. As presented in Fig. 3(e), the weightlessness process can be divided into three stages. Only a small amount of weight loss appears from room temperature to 300 °C, which is mainly caused by the

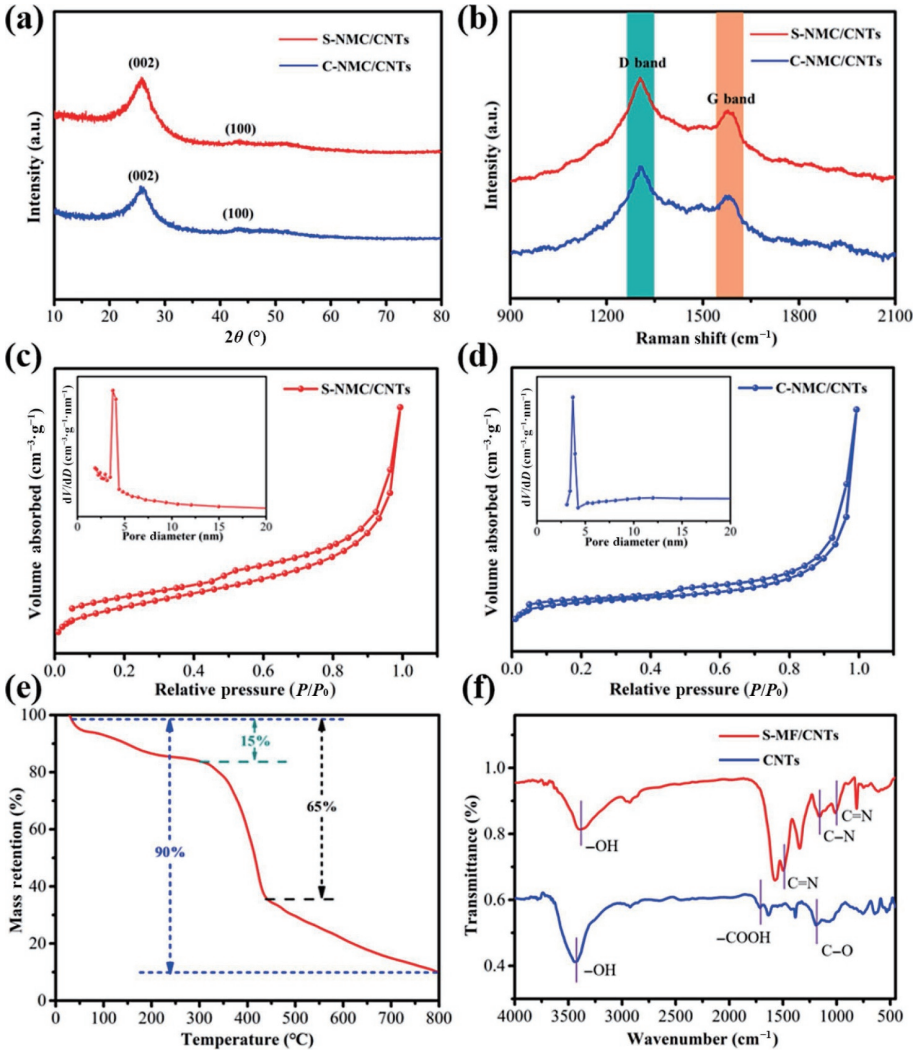

Figure 3 (a) XRD patterns and (b) Raman spectra of S-NMC/CNTs and C-NMC/CNTs. N_2 adsorption/desorption isotherms and corresponding pore size distribution curves (insets) of (c) S-NMC/CNTs and (d) C-NMC/CNTs. (e) TGA curve of S-MF/CNTs. (f) FT-IR spectra of S-MF/CNTs and CNTs.

evaporation of surface moisture or decomposition of unpolymerized oligomers. There is a sharp weight loss from 300 to 440 °C, corresponding to the rapid decomposition of the MF resin. In the third stage, the weight loss phenomenon gradually decreases with the increase of temperature, which can be due to the break of ether bonds in the MF resin large molecule [35]. To better observe the structural changes of the materials obtained at different carbonization temperatures, TEM images were further provided. As shown in Fig. S3(a) in the ESM, the resulting product carbonized at 300 °C has no significant change compared with that of as-synthesized samples. This result suggests that low temperature is insufficient to decompose the MF resin. When the carbonization temperature increased to 500 °C, the obtained product displays significant structural shrinkage, and the diameter of the 1D composite largely decreases from 82 to 42 nm, showing a shrinkage rate of 49% (Figs. S3(b) and S4 in the ESM). The mesoporous structure is seriously damaged as the temperature rises to 600 °C (Fig. S3(c) in the ESM). When the carbonization temperature further increased to 800 °C, the diameter of the composite is directly reduced to about 20 nm, indicating that only CNTs are basically reserved (Fig. S3(d) in the ESM). Figure S4 in the ESM displays the statistics of the corresponding volume shrinkage rates of S-MF/CNTs at different carbonization temperatures. It can be clearly seen that the volume shrinkage of S-MF/CNTs composite significantly increases with the increase of the thermal treatment temperature, indicating that the stability is greatly affected by the carbonization temperature. These are almost consistent with TGA results. Thus, to ensure the integrity of the porous structure and simultaneously ensure the electrical conductivity of the material, the optimum carbonization temperature is determined to be 500 °C.

To explore the assembly mechanism of the composites, the influence of the CNT amounts on the assembly was further investigated. Firstly, only mesoporous MF spheres are obtained in the absence of CNTs (Fig. S5(a) in the ESM), suggesting the support effect of CNTs. When 10 mg of CNTs were added, the obtained product shows the 1D core–shell mesoporous structure (Fig. S5(b) in the ESM), however, the thickness of MF is too thick and the morphology is uneven. If the quantity of CNTs is increased to 14 mg, mesoporous MF resin cannot uniformly grow onto the surface of CNTs (Fig. S5(d) in the ESM).

The interfacial interactions between CNTs and MF monomers were then investigated by measuring the surface electrical properties (Table S1 in the ESM). The zeta-potential of CNTs is −19.8 mV and basically unchanged after adding P123/F127 mixed surfactant, because P123/F127 is a non-ionic surfactant. However, the zeta-potential of CNTs/F127/P123/MF is neutralized from −19.8 to −0.3 mV after MF resin oligomer was added because of the positive charge of MF (11.8 mV). These results indicate that electrostatic interaction is one of the main assembly forces in the NMC/CNTs composites.

FT-IR spectra were also conducted to monitor the chemical changes during the assembly process (Fig. 3(f)). For CNTs, the characteristic peaks at about 1718 and 1190 cm^{-1} belong to the

stretching vibrations of –COOH and C–O, respectively. And the obvious characteristic peak of –OH at 3442 cm^{-1} is detected. This means that there are amount of oxygen-containing functional groups on the CNT surface. Compared with pure CNTs, a new characteristic peak appears at about 1182 cm^{-1} for S-MF/CNTs, which belongs to the aromatic C–N stretching vibration mode. Besides, the characteristic peaks of triazine ring are also found at 1483 and 810 cm^{-1} [36]. The above results indicate that an effective co-assembly has occurred among CNTs, micelle, and MF resin. Moreover, the characteristic peak of –OH shifts from 3442 to 3386 cm^{-1}, indicating the formation of H-bond among CNTs, micelle, and MF resin. In addition, to explore the role of oxygen-containing functional groups in the assembly process, the sample was also prepared by using pristine CNTs as the support while keeping other parameters unchanged. As observed in Fig. S6(a) in the ESM, only a small part of MF resin adsorbed onto the surface of pristine CNTs. This is mainly due to the reason that the surface of pristine CNTs has a fewer oxygen-containing functional groups (Fig. S6(b) in the ESM). This suggests that oxygen-containing functional groups also play a crucial role in the assembly process, and a large number of oxygen-containing functional groups can provide strong assembling hydrogen bond forces.

In order to understand the evolution mechanism of the pore structure, the effect of different P123/F127 mass ratios on the pore structure of MF/CNTs composites was investigated in detail. When the P123/F127 mass ratio decreased to 1:2, the MF/CNTs product retains the spherical mesoporous structure and the diameter increases to 113 nm (Fig. S7(a) in the ESM). Furthermore, the diameter further increases to 202 nm, when only F127 is used as the surfactant, where the product also exhibits the spherical mesoporous structure (Fig. S7(b) in the ESM). Such results indicate that the properties of surfactants can also affect the assembly force. Compared with P123, F127 possesses the same hydrophobic moieties but longer hydrophilic chains. So, the hydrophilic and hydrophobic ratio of surfactants in the system can be changed by tuning the P123/F127 mass ratio, which in turn affects the assembly process and the structure of pores. To confirm the above deduction, F108 with longer hydrophilic chains is used instead of F127 while keeping the P123/F108 mass ratio to 1:1. TEM image clearly shows the patterning of closely arranged spherical pores onto the surfaces of CNTs, and the diameter of the obtained product increases to 185 nm (Fig. S7(c) in the ESM), demonstrating the important role of hydrophilic and hydrophobic ratio of surfactant in the assembly process. Additionally, the MF/CNTs composite with non-porous structure was also prepared without any surfactants following the above strategy (Fig. S7(d) in the ESM), further confirming the pore-forming effect of surfactants. These results fully illustrate that the pore structure and the assembly force can be simply and effectively controlled by changing the P123/F127 mass ratio.

According to the above observations, we propose a possible formation mechanism of NMC/CNTs composites with different pore structures, which is basically a co-assembly process guided by the surfactants (see Fig. 1). Firstly, triblock copolymers formed the micelles with PPO as core and PEO as corona in aqueous solution at 40 °C [37–39]. Here, the structures of micelles are determined by the packing parameter $P = V_0/(a_0 l_c)$, where V_0 and l_c are the volume and length of the hydrophobic block, a_0 represents the contact area of the hydrophilic block [40, 41]. When P123 and F127 are used as co-surfactants, the spherically structured micelles were formed because of the lower hydrophobic/hydrophilic ratio, causing the $P \leq 1/3$ (route A). However, if only P123 was used as the template, the larger hydrophobic/hydrophilic ratio of P123 caused $1/3 < P \leq 1/2$, thus resulting in the formation of micelles with cylindrical structure (route B). Meanwhile, melamine reacts with formaldehyde under weak alkaline conditions to form water-soluble oligomers, which are used as the precursors (Fig. S8 in the ESM) [41]. After CNTs and as-prepared oligomers were added to the above micelle solution, the co-assembly occurs among micelles, CNTs, and oligomers via electrostatic and hydrogen bond interactions. Under the catalysis of HCl, the oligomers begin to polymerize and gradually transform into MF resin with the increase of reaction time, thus obtaining the mesoporous MF/CNTs composites with spherical pore or cylindrical pore. Herein, the pore size of mesoporous materials mainly depends on the length of the hydrophobic block of the surfactant, so the pore size of the products decreased with the decrease of the hydrophobic and hydrophilic ratio of the surfactants [42]. On the other hand, due to the increase of the hydrophilic block, the assembly force among micelles, MF oligomers, and CNTs template can be effectively increased, so the diameter of 1D composites increased [43]. Finally, the NMC/CNTs composites with controlled pore structure are prepared after carbonization at optimized temperature in nitrogen atmosphere.

To verify the universality of our proposed assembly strategy, micron-sized SiO block, submicron Fe_2O_3 ellipsoid, 2D graphene nanosheet, and carbon nanosphere (C) were selected as the different substrates to replace CNTs for the controllable assembly. As can be seen from Fig. 4, we successfully assembled spherical pore structured mesoporous MF onto SiO and elliptical Fe_2O_3 (Figs. 4(e) and 4(f)). Besides, the mesoporous MF with cylindrical pore structure is also well grown onto 2D graphene oxide (GO) and carbon nanospheres (Figs. 4(g) and 4(h)). The above results fully indicate that the co-assembly strategy proposed in our work is universal and independent of the composition, dimension, and size of the substrates.

Two NMC/CNTs composites with different pore structures

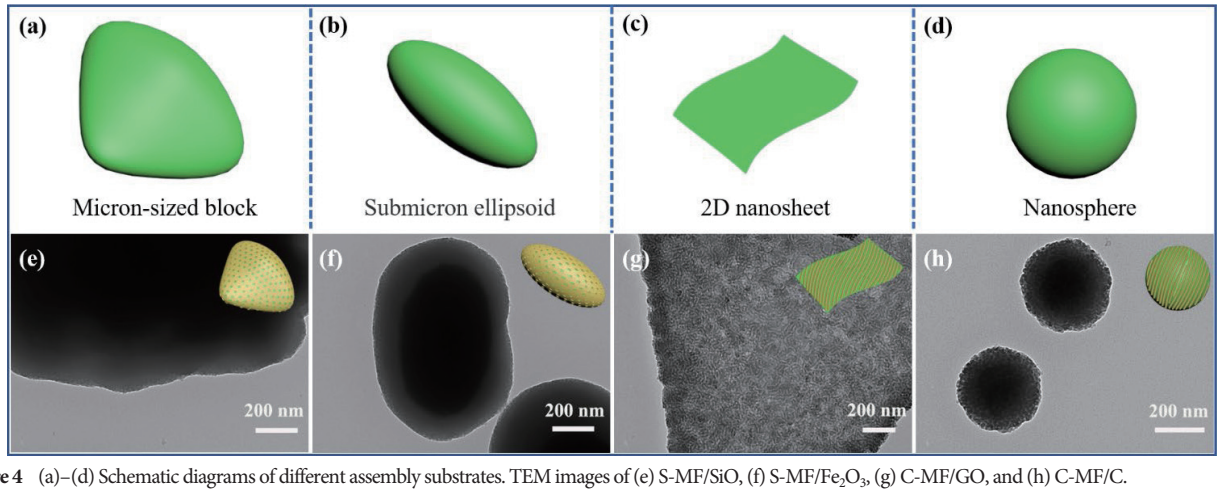

Figure 4 (a)–(d) Schematic diagrams of different assembly substrates. TEM images of (e) S-MF/SiO, (f) S-MF/Fe_2O_3, (g) C-MF/GO, and (h) C-MF/C.

were employed as the anode materials for LIBs, and then we systemically investigated the effect of pore structure on their lithium storage performance. Figure 5(a) shows the CV curves of the first three cycles of the S-NMC/CNTs electrode in LIBs with a sweep speed of 0.1 mV·s^{-1}. The CV curve of the first cycle exhibits a broad cathodic peak at 0.5–1.2 V, which disappeared in the second cycle. This phenomenon indicates that the obtained anode material has an irreversible initial capacity, which is ascribed to the generation of a solid electrolyte interface (SEI) film and the decomposition of the electrolyte. The weak broad peak at 1.1 V during charge stage can be assigned to the delithiation [44]. In addition, the almost overlapped CV curves of the second and third cycles reveal the excellent reversibility of the S-NMC/CNTs electrode. For C-NMC/CNTs electrode, it shows the similar CV curves to S-NMC/CNTs electrode, demonstrating the similar Li ion storage behavior (Fig. S9 in the ESM).

The galvanostatic discharge–charge profiles of S-NMC/CNTs for the first, second, third, and 100th cycles at a current density of 0.1 A·g^{-1} are shown in Fig. S10(a) in the ESM. The initial discharge specific capacity can reach 1173.2 mAh·g^{-1} and charge capacity was about 726.2 mAh·g^{-1}, showing an initial Coulombic efficiency (ICE) of about 61.9%. The irreversible capacity is mainly caused by the large amount of Li consumed during the formation of SEI films. However, the S-NMC/CNTs electrode shows the excellent reversible capacity at the second, third, and even the 100th cycles, the Coulombic efficiency can reach 99% at the 100th cycle. Figure S10(b) in the ESM shows that the C-NMC/CNTs electrode has the similar charge–discharge curves to S-NMC/CNTs, indicating that the electrochemical reaction types of electrode materials are roughly the same. The initial discharge specific capacity of C-NMC/CNTs electrode is about 1171.8 mAh·g^{-1}, basically the same as that of S-NMC/CNTs electrode. However, the charge specific capacity is only 658.8 mAh·g^{-1}, corresponding to ICE of 56.2%. The lower ICE of C-NMC/CNTs electrode can be attributed to the larger surface area, and the cylindrical pore structure has more open space, leading to the occurrence of more side reactions.

Figure 5(b) displays the cycling stability of three electrodes at the current density of 0.1 A·g^{-1}. Both S-NMC/CNTs and C-NMC/CNTs electrodes demonstrate the excellent cycling stability, and the reversible capacities still retain as 588.1 and 540 mAh·g^{-1} after 100 cycles, respectively. The lower reversible capacity of C-NMC/CNTs electrode can be due to the more surface side reactions caused by cylindrical pore structure. This result is consistent with the above galvanostatic discharge–charge analysis. However, the reversible capacity of carbon materials with non-pore structure (NC/CNTs) is only 148 mAh·g^{-1} after 100 cycles at 0.1 A·g^{-1}, confirming that the mesopore structure presents unique structural advantages in energy storage.

The rate performances of three anodes including S-NMC/CNTs, C-NMC/CNTs, and NC/CNTs were measured at different current densities between 0.1 and 2 A·g^{-1} (Fig. 5(c)). Obviously, the S-NMC/CNTs electrode has the highest capacity at each current density. The reversible capacities of S-NMC/CNTs are 582, 468.6, 362.9, 293.6, and 247.7 mAh·g^{-1} at the current densities of 0.1, 0.2, 0.5, 1, and 2 A·g^{-1}, respectively. When the current density returns to 0.1 A·g^{-1} again after 50 cycles at different rates, the discharge specific capacity still recovers to 588.5 mAh·g^{-1}, indicating an excellent cycling and rate performance. The energy storage performance of S-NMC/CNTs electrode developed in our work is superior to most previously reported carbon-based anode materials (Fig. 5(d) and Table S2 in the ESM) [44–53].

The long-term cycling stability of two electrodes under high

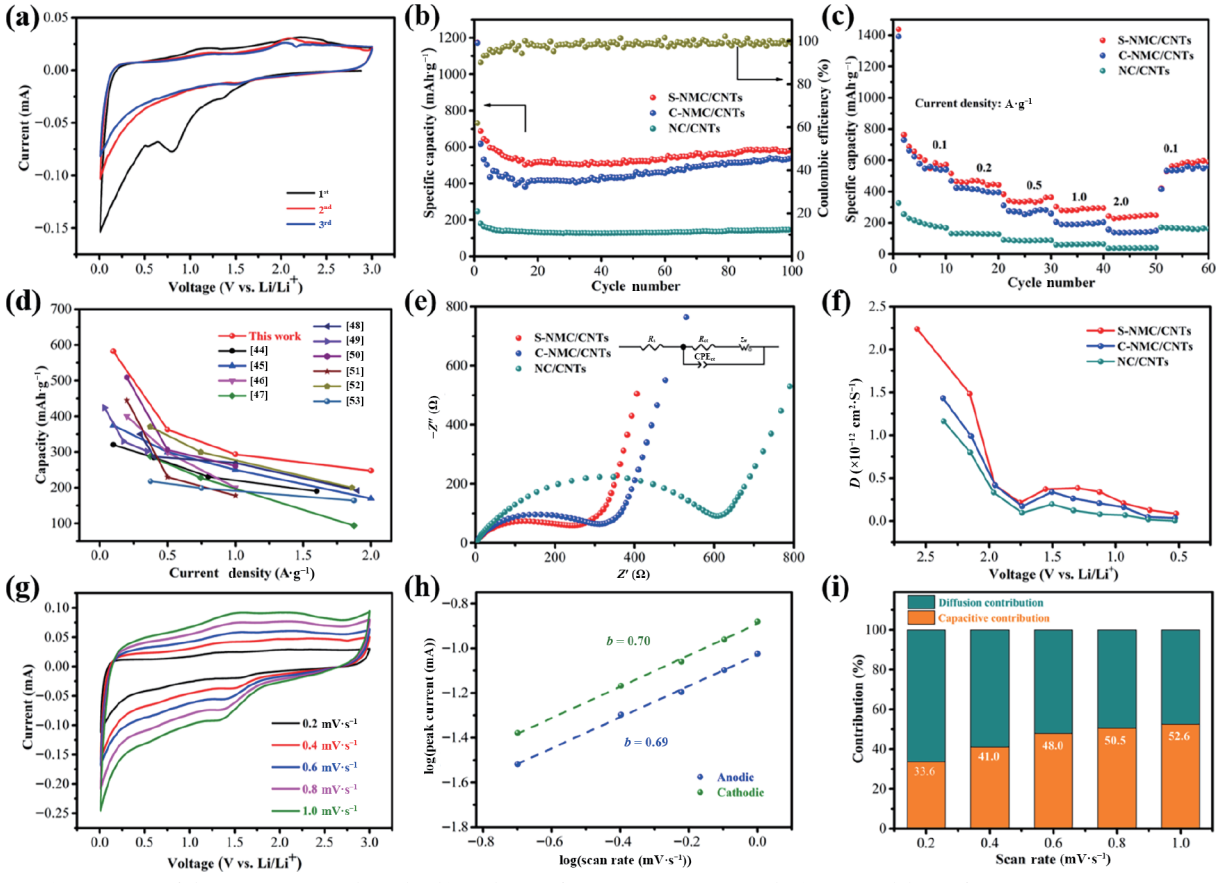

Figure 5 (a) CV curves of the S-NMC/CNTs electrode. (b) Cycling performances at 0.1 A·g^{-1} and (c) rate capabilities of S-NMC/CNTs, C-NMC/CNTs, and NC/CNTs electrodes. (d) Comparison of the reversible capacity between S-NMC/CNTs and different carbon-based electrodes in the previous literatures. (e) EIS spectra and (f) Li diffusion coefficients of S-NMC/CNTs, C-NMC/CNTs, and NC/CNTs electrodes. (g) CV profiles of S-NMC/CNTs at 0.2–1.0 mV·s^{-1}, (h) relationship between the log(*i*) and log(*v*), and (i) the percentages of capacitive- and diffusion-controlled capacities at different scan rates of S-NMC/CNTs.

current density is a key factor in practical applications. Figure S11 in the ESM displays the cycling profiles of S-NMC/CNTs and C-NMC/CNTs at the current density of 2 $A \cdot g^{-1}$. After 650 cycles, the reversible capacities still retain as 316 and 284.1 $mAh \cdot g^{-1}$ for S-NMC/CNTs and C-NMC/CNTs, respectively, indicating that obtained mesoporous carbon electrode materials deliver the excellent long-term cycle stability at high current density. Meanwhile, to better show the structural stability of the S-NMC/CNTs electrode, its morphology after cycling was further characterized. As seen from Fig. S12 in the ESM, no serious cracking or pulverization is observed and the 1D structure remains well after cycling, suggesting a good structural stability.

The EIS spectra of S-NMC/CNTs, C-NMC/CNTs, and NC/CNTs electrodes were then analyzed for better understanding of their diffusion kinetics. Figure 5(e) clearly shows that the S-NMC/CNTs and C-NMC/CNTs have smaller concave semicircles at the high frequency range than that of NC/CNTs, indicating that mesoporous structure can effectively improve the electron transfer rate. Besides, the smallest concave semicircle is from the S-NMC/CNTs electrode, suggesting that the spherical mesopore has the fastest charge diffusion kinetics.

The chemical diffusion coefficient (D) of Li ions largely determines the reaction rate, thus affecting the overall performance of the battery. Therefore, it is important to determine the chemical diffusion coefficient of electrodes. Here, the D value based on galvanostatic intermittent titration (GITT) results (Fig. S13(a) in the ESM) is calculated according to Eq. (1)

$$D = \frac{4}{\pi\tau}\left(\frac{m_B V_m}{M_B S}\right)^2 \left(\frac{\Delta E_s}{\Delta E_\tau}\right)^2 \quad (1)$$

where ΔE_s is change in steady state potential before and after current pulse, ΔE_τ is change in potential during current pulse, τ represents current pulse duration, m_B represents active mass, S is electrode–electrolyte interface area, and V_m and M_B indicate the molar volume and molar mass of the compound, respectively. The D values of S-NMC/CNTs and C-NMC/CNTs are calculated to be 0.08 to 2.24×10^{-12} and 0.03 to 1.43×10^{-12}, respectively, which are significantly higher than that of NC/CNTs (0.002 to 1.24×10^{-12}) (Fig. 5(f)). This result further proves that the mesoporous structure can effectively improve the diffusivity of Li ions, and the spherical pore can provide the faster transfer kinetics of ions.

In order to explore Li^+ storage kinetics of S-NMC/CNTs, CV measurements were performed at different scan rates (v) from 0.2 to 1 $mV \cdot s^{-1}$. Figure 5(g) demonstrates the similar CV loops at different scan rates, indicating a good electrochemical stability of S-NMC/CNTs electrode. In general, scan rate and test current (i) obey the following relationship

$$i = av^b \quad (2)$$

where a and b are adjustable values. Generally, when b = 0.5, the electrochemical reaction of the electrode is mainly a diffusion-controlled process, while b = 1 corresponding to the capacitive-dominated behavior. The b values of S-NMC/CNTs electrode are calculated to be 0.70 and 0.69 for cathodic and anodic processes, respectively (Fig. 5(h)). This result indicates that the electrochemical process of S-NMC/CNTs electrode is controlled by both diffusion and capacitive. Additionally, the relative contributions from capacitive behavior (k_1v) and diffusion behavior ($k_2v^{1/2}$) at fixed potentials can be obtained by Eq. (3)

$$i(v) = k_1 v + k_2 v^{1/2} \quad (3)$$

As shown in Fig. 5(i), the capacitance contribution increases with the increase of scanning speed for S-NMC/CNTs, and the capacitance contribution of S-NMC/CNTs electrode reaches 52.6% when the sweep speed was 1 $mV \cdot s^{-1}$ (Fig. S13(b) in the ESM).

Figure 6 depicts the different transport pathways of electrons/ions in the S-NMC/CNTs and C-NMC/CNTs electrodes. In brief, 1D structure of CNTs can provide a fast electron transfer rate due to the large aspect ratio. Besides, mesoporous structure, especially spherical pore, can not only effectively promote the penetration of electrolyte and provide more electrochemical active sites, but also shorten the diffusion distance of electrons/ions, thereby greatly boosting their electrochemical performance.

4 Conclusions

In summary, nitrogen-doped mesoporous carbon materials with spherical and cylindrical pore structures have been successfully assembled onto carbon nanotubes via a facile cooperative assembly process assisted by triblock P123 and F127 copolymers. After systematically exploring the assembly process, it is found that the properties of copolymers play a crucial role in the pore structures of NMC/CNTs. Moreover, the assembly force can also be well tuned via adjusting the hydrophobic/hydrophilic ratio of

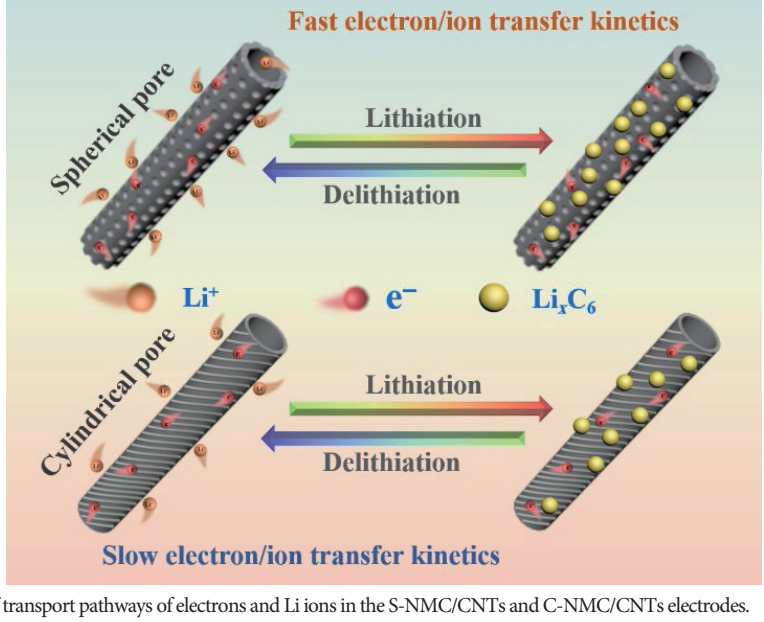

Figure 6 Schematic illustration of transport pathways of electrons and Li ions in the S-NMC/CNTs and C-NMC/CNTs electrodes.

surfactants. More importantly, the co-assembly strategy proposed in this work is universal and independent of the composition, dimension, and size of the substrates. Benefitting from the fast electrons/ions diffusion kinetics, the S-NMC/CNTs anode with spherical pore structure delivers a superior lithium storage performance with a high reversible capacity of 588.1 $mAh \cdot g^{-1}$ after 100 cycles at the current density of 0.1 $A \cdot g^{-1}$.

Acknowledgements

The authors thank the support from the Shuguang Program supported by Shanghai Education Development Foundation and Shanghai Municipal Education Commission (No. 18SG35), the Basic Research Program of Shanghai Municipal Government (No. 21JC1406002), and the Shanghai Engineering Research Center of Advanced Thermal Functional Materials (Shanghai Polytechnic University).

Electronic Supplementary Material: Supplementary material (SEM and TEM images, EDX patterns, statistics of corresponding shrinkage rates, zeta-potential comparisons, FT-IR spectra, electrochemical tests, performance comparison) is available in the online version of this article at https://doi.org/10.1007/s12274-023-5540-2.

References

[1] Li, M.; Lu, J.; Chen, Z. W.; Amine, K. 30 years of lithium-ion batteries. *Adv. Mater.* **2018**, *30*, 1800561.

[2] Sun, Y. M.; Liu, N.; Cui, Y. Promises and challenges of nanomaterials for lithium-based rechargeable batteries. *Nat. Energy* **2016**, *1*, 16071.

[3] Goodenough, J. B.; Park, K. S. The Li-ion rechargeable battery: A perspective. *J. Am. Chem. Soc.* **2013**, *135*, 1167–1176.

[4] Geng, H. Y.; Peng, Y.; Qu, L. T.; Zhang, H. J.; Wu, M. H. Structure design and composition engineering of carbon-based nanomaterials for lithium energy storage. *Adv. Energy Mater.* **2020**, *10*, 1903030.

[5] Kim, M. S.; Bhattacharjya, D.; Fang, B. Z.; Yang, D. S.; Bae, T. S.; Yu, J. S. Morphology-dependent Li storage performance of ordered mesoporous carbon as anode material. *Langmuir* **2013**, *29*, 6754–6761.

[6] He, F. Y.; Tang, C.; Zhu, G. J.; Liu, Y. D.; Du, A. J.; Zhang, Q. B.; Wu, M. H.; Zhang, H. J. Leaf-inspired design of mesoporous Sb_2S_3/N-doped $Ti_3C_2T_x$ composite towards fast sodium storage. *Sci. China Chem.* **2021**, *64*, 964–973.

[7] Xu, W. L.; Tang, C.; Huang, N.; Du, A. J.; Wu, M. H.; Zhang, J. J.; Zhang, H. J. Adina rubella-like microsized SiO@N-doped carbon grafted with N-doped carbon nanotubes as anodes for high-performance lithium storage. *Small Sci.* **2022**, *2*, 2100105.

[8] Ma, T. Y.; Liu, L.; Yuan, Z. Y. Direct synthesis of ordered mesoporous carbons. *Chem. Soc. Rev.* **2013**, *42*, 3977–4003.

[9] Guo, D. Y.; Fu, Y. B.; Bu, F. X.; Liang, H. C.; Duan, L. L.; Zhao, Z. W.; Wang, C. Y.; El-Toni, A. M.; Li, W.; Zhao, D. Y. Monodisperse ultrahigh nitrogen-containing mesoporous carbon nanospheres from melamine-formaldehyde resin. *Small Methods* **2021**, *5*, 2001137.

[10] Septani, C. M.; Wang, C. A.; Jeng, U. S.; Su, Y. C.; Ko, B. T.; Sun, Y. S. Hierarchically porous carbon materials from self-assembled block copolymer/dopamine mixtures. *Langmuir* **2020**, *36*, 11754–11764.

[11] Peng, L.; Peng, H. R.; Hung, C. T.; Guo, D. Y.; Duan, L. L.; Ma, B.; Liu, L. L.; Li, W.; Zhao, D. Y. Programmable synthesis of radially gradient-structured mesoporous carbon nanospheres with tunable core–shell architectures. *Chem* **2021**, *7*, 1020–1032.

[12] Liu, Z. H.; Du, Y.; Zhang, P. F.; Zhuang, Z. C.; Wang, D. S. Bringing catalytic order out of chaos with nitrogen-doped ordered mesoporous carbon. *Matter* **2021**, *4*, 3161–3194.

[13] Zhang, Y. Z.; Chen, L.; Meng, Y.; Xie, J.; Guo, Y.; Xiao, D. Lithium and sodium storage in highly ordered mesoporous nitrogen-doped carbons derived from honey. *J. Power Sources* **2016**, *335*, 20–30.

[14] Wang, J.; Chang, Z.; Ding, B.; Li, T.; Yang, G. L.; Pang, Z. B.; Nakato, T.; Eguchi, M.; Kang, Y. M.; Na, J. et al. Universal access to two-dimensional mesoporous heterostructures by micelle-directed interfacial assembly. *Angew. Chem., Int. Ed.* **2020**, *59*, 19570–19575.

[15] Wang, L.; Du, Z.; Xiang, L. X.; Hou, D.; Zhu, S. H.; Zhu, J. F.; Mai, Y. Y.; Che, R. C. The ordered mesoporous carbon coated graphene as a high-performance broadband microwave absorbent. *Carbon* **2021**, *179*, 435–444.

[16] Wang, R. C.; Lan, K.; Lin, R. F.; Jing, X. X.; Hung, C. T.; Zhang, X. M.; Liu, L. L.; Yang, Y.; Chen, G.; Liu, X. G. et al. Precisely controlled vertical alignment in mesostructured carbon thin films for efficient electrochemical sensing. *ACS Nano* **2021**, *15*, 7713–7721.

[17] Fang, Y.; Lv, Y. Y.; Tang, J.; Wu, H.; Jia, D. S.; Feng, D.; Kong, B.; Wang, Y. C.; Elzatahry, A. A.; Al-Dahyan, D. et al. Growth of single-layered two-dimensional mesoporous polymer/carbon films by self-assembly of monomicelles at the interfaces of various substrates. *Angew. Chem., Int. Ed.* **2015**, *54*, 8425–8429.

[18] Dong, R. H.; Zhang, T.; Feng, X. L. Interface-assisted synthesis of 2D materials: Trend and challenges. *Chem. Rev.* **2018**, *118*, 6189–6235.

[19] Tu, S. B.; Su, H.; Sui, D.; He, Y. W.; Cheng, M. R.; Bai, P. X.; Zhang, C.; Sun, P. F.; Wang, C. H.; Jiang, J. X. et al. Mesoporous carbon nanomaterials with tunable geometries and porous structures fabricated by a surface-induced assembly strategy. *Energy Storage Mater.* **2021**, *35*, 602–609.

[20] Culebras, M.; Geaney, H.; Beaucamp, A.; Upadhyaya, P.; Dalton, E.; Ryan, K. M.; Collins, M. N. Bio-derived carbon nanofibres from lignin as high-performance Li-ion anode materials. *ChemSusChem* **2019**, *12*, 4516–4521.

[21] Liu, X. M.; Huang, Z. D.; Oh, S. W.; Zhang, B.; Ma, P. C.; Yuen, M. M. F.; Kim, J. K. Carbon nanotube (CNT)-based composites as electrode material for rechargeable Li-ion batteries: A review. *Compos. Sci. Technol.* **2012**, *72*, 121–144.

[22] Liu, S. H.; Gordiichuk, P.; Wu, Z. S.; Liu, Z. Y.; Wei, W.; Wagner, M.; Mohamed-Noriega, N.; Wu, D. Q.; Mai, Y. Y.; Herrmann, A. et al. Patterning two-dimensional free-standing surfaces with mesoporous conducting polymers. *Nat. Commun.* **2015**, *6*, 8817.

[23] Xu, Y.; Zhang, C. L.; Zhou, M.; Fu, Q.; Zhao, C. X.; Wu, M. H.; Lei, Y. Highly nitrogen doped carbon nanofibers with superior rate capability and cyclability for potassium ion batteries. *Nat. Commun.* **2018**, *9*, 1720.

[24] Wang, N.; Hou, D.; Li, Q.; Zhang, P. F.; Wei, H.; Mai, Y. Y. Two-dimensional interface engineering of mesoporous polydopamine on graphene for novel organic cathodes. *ACS Appl. Energy Mater.* **2019**, *2*, 5816–5823.

[25] Tian, H.; Zhu, S. Y.; Xu, F. G.; Mao, W. T.; Wei, H.; Mai, Y. Y.; Feng, X. L. Growth of 2D mesoporous polyaniline with controlled pore structures on ultrathin MoS_2 nanosheets by block copolymer self-assembly in solution. *ACS Appl. Mater. Interfaces* **2017**, *9*, 43975–43982.

[26] Lin, T. Q.; Chen, I. W.; Liu, F. X.; Yang, C. Y.; Bi, H.; Xu, F. F.; Huang, F. Q. Nitrogen-doped mesoporous carbon of extraordinary capacitance for electrochemical energy storage. *Science* **2015**, *350*, 1508–1513.

[27] Xia, S. S.; Wang, Y. R.; Liu, Y.; Wu, C. H.; Wu, M. H.; Zhang, H. J. Ultrathin MoS_2 nanosheets tightly anchoring onto nitrogen-doped graphene for enhanced lithium storage properties. *Chem. Eng. J.* **2018**, *332*, 431–439.

[28] Tan, H. B.; Tang, J.; Henzie, J.; Li, Y. Q.; Xu, X. T.; Chen, T.; Wang, Z. L.; Wang, J. Y.; Ide, Y.; Bando, Y. et al. Assembly of hollow carbon nanospheres on graphene nanosheets and creation of iron–nitrogen-doped porous carbon for oxygen reduction. *ACS Nano* **2018**, *12*, 5674–5683.

[29] Liu, Z. H.; Du, Y.; Yu, R. H.; Zheng, M. B.; Hu, R.; Wu, J. S.; Xia, Y. Y.; Zhuang, Z. C.; Wang, D. S. Tuning mass transport in electrocatalysis down to sub-5 nm through nanoscale grade separation. *Angew. Chem., Int. Ed.* **2023**, *62*, e202212653.

[30] Zhang, B. T.; Wang, Q.; Zhang, Y.; Teng, Y. G.; Fan, M. H. Degradation of ibuprofen in the carbon dots/Fe_3O_4@carbon sphere

pomegranate-like composites activated persulfate system. *Sep. Purif. Technol.* **2020**, *242*, 116820.
[31] Wang, W.; Zhou, J. H.; Wang, Z. P.; Zhao, L. Y.; Li, P. H.; Yang, Y.; Yang, C.; Huang, H. X.; Guo, S. J. Short-range order in mesoporous carbon boosts potassium-ion battery performance. *Adv. Energy Mater.* **2018**, *8*, 1701648.
[32] Cao, B.; Zhang, Q.; Liu, H.; Xu, B.; Zhang, S. L.; Zhou, T. F.; Mao, J. F.; Pang, W. K.; Guo, Z. P.; Li, A. et al. Graphitic carbon nanocage as a stable and high power anode for potassium-ion batteries. *Adv. Energy Mater.* **2018**, *8*, 1801149.
[33] Zhang, H. J.; Li, Z. Y.; Xu, P. P.; Wu, R. F.; Jiao, Z. A facile two step synthesis of novel chrysanthemum-like mesoporous silicananoparticles for controlled pyrene release. *Chem. Commun.* **2010**, *46*, 6783–6785.
[34] Liu, J.; Yang, T. Y.; Wang, D. W.; Lu, G. Q.; Zhao, D. Y.; Qiao, S. Z. A facile soft-template synthesis of mesoporous polymeric and carbonaceous nanospheres. *Nat. Commun.* **2013**, *4*, 2798.
[35] Zhang, R.; Liu, Z. L.; Gao, T. N.; Zhang, L. L.; Zheng, Y. N.; Zhang, J. N.; Zhang, L.; Qiao, Z. A. A solvent-polarity-induced interface self-assembly strategy towards mesoporous triazine-based carbon materials. *Angew. Chem., Int. Ed.* **2021**, *60*, 24299–24305.
[36] Merline, D. J.; Vukusic, S.; Abdala, A. A. Melamine formaldehyde: Curing studies and reaction mechanism. *Polym. J.* **2013**, *45*, 413–419.
[37] Tian, H.; Qin, J. Q.; Hou, D.; Li, Q.; Li, C.; Wu, Z. S.; Mai, Y. Y. General interfacial self-assembly engineering for patterning two-dimensional polymers with cylindrical mesopores on graphene. *Angew. Chem., Int. Ed.* **2019**, *58*, 10173–10178.
[38] Chaibundit, C.; Ricardo, N. M. P. S.; De M. L. L. Costa, F.; Yeates, S. G.; Booth, C. Micellization and gelation of mixed copolymers P123 and F127 in aqueous solution. *Langmuir* **2007**, *23*, 9229–9236.
[39] Lam, Y. M.; Grigorieff, N.; Goldbeck-Wood, G. Direct visualisation of micelles of pluronic block copolymers in aqueous solution by cryo-TEM. *Phys. Chem. Chem. Phys.* **1999**, *1*, 3331–3334.
[40] Mai, Y. Y.; Eisenberg, A. Self-assembly of block copolymers. *Chem. Soc. Rev.* **2012**, *41*, 5969–5985.
[41] Li, C.; Li, Q.; Kaneti, Y. V.; Hou, D.; Yamauchi, Y.; Mai, Y. Y. Self-assembly of block copolymers towards mesoporous materials for energy storage and conversion systems. *Chem. Soc. Rev.* **2020**, *49*, 4681–4736.
[42] Zhang, L. L.; Wang, T.; Gao, T. N.; Xiong, H. L.; Zhang, R.; Liu, Z. L.; Song, S. Y.; Dai, S.; Qiao, Z. A. Multistage self-assembly strategy: Designed synthesis of N-doped mesoporous carbon with high and controllable pyridine N content for ultrahigh surface-area-normalized capacitance. *CCS Chem.* **2020**, *3*, 870–881.
[43] Wang, C. Y.; Wan, X. Y.; Duan, L. L.; Zeng, P. Y.; Liu, L. L.; Guo, D. Y.; Xia, Y.; Elzatahry, A. A.; Xia, Y. Y.; Li, W. et al. Molecular design strategy for ordered mesoporous stoichiometric metal oxide. *Angew. Chem., Int. Ed.* **2019**, *58*, 15863–15868.
[44] Yin, H.; Li, Q. W.; Cao, M. L.; Zhang, W.; Zhao, H.; Li, C.; Huo, K. F.; Zhu, M. Q. Nanosized-bismuth-embedded 1D carbon nanofibers as high-performance anodes for lithium-ion and sodium-ion batteries. *Nano Res.* **2017**, *10*, 2156–2167.
[45] Wu, X. L.; Liu, Q.; Guo, Y. G.; Song, W. G. Superior storage performance of carbon nanosprings as anode materials for lithium-ion batteries. *Electrochem. Commun.* **2009**, *11*, 1468–1471.
[46] Wang, F. F.; Song, R. R.; Song, H. H.; Chen, X. H.; Zhou, J. S.; Ma, Z. K.; Li, M. C.; Lei, Q. Simple synthesis of novel hierarchical porous carbon microspheres and their application to rechargeable lithium-ion batteries. *Carbon* **2015**, *81*, 314–321.
[47] Wang, L. P.; Schütz, C.; Salazar-Alvarez, G.; Titirici, M. M. Carbon aerogels from bacterial nanocellulose as anodes for lithium ion batteries. *RSC Adv.* **2014**, *4*, 17549–17554.
[48] Saravanan, K. R.; Kalaiselvi, N. Nitrogen containing bio-carbon as a potential anode for lithium batteries. *Carbon* **2015**, *81*, 43–53.
[49] Li, M. Y.; Wu, Y.; Zhao, F.; Wei, Y.; Wang, J. P.; Jiang, K. L.; Fan, S. S. Cycle and rate performance of chemically modified super-aligned carbon nanotube electrodes for lithium ion batteries. *Carbon* **2014**, *69*, 444–451.
[50] Zhang, W. L.; Yin, J.; Lin, Z. Q.; Lin, H. B.; Lu, H. Y.; Wang, Y.; Huang, W. M. Facile preparation of 3D hierarchical porous carbon from lignin for the anode material in lithium ion battery with high rate performance. *Electrochim. Acta* **2015**, *176*, 1136–1142.
[51] Lei, W.; Han, L. L.; Xuan, C. J.; Lin, R. Q.; Liu, H. F.; Xin, H. L.; Wang, D. L. Nitrogen-doped carbon nanofibers derived from polypyrrole coated bacterial cellulose as high-performance electrode materials for supercapacitors and Li-ion batteries. *Electrochim. Acta* **2016**, *210*, 130–137.
[52] Tang, K.; White, R. J.; Mu, X. K.; Titirici, M. M.; Van Aken, P. A.; Maier, J. Hollow carbon nanospheres with a high rate capability for lithium-based batteries. *ChemSusChem* **2012**, *5*, 400–403.
[53] Wang, L. P.; Schnepp, Z.; Titirici, M. M. Rice husk-derived carbon anodes for lithium ion batteries. *J. Mater. Chem. A* **2013**, *1*, 5269–5273.